JOURNAL of the MEXICAN CHEMICAL SOCIETY

https://www.jmcs.org.mx/

Article

Open Access

J. Mex. Chem. Soc. **2026**, *70(1):e2490*

Received May 24th, 2025
Accepted October 13th, 2025

http://dx.doi.org/10.29356/jmcs.v70i1.2490
e-location ID: 2490

Keywords:
Alloy, Pd, hydrogenation

Palabras clave:
Aleación, Pd, hidrogenación

***Corresponding author:**
Li Jiang
email: jiangli@cjlu.edu.cn
Yahong Luo
email: yhluo2403@163.com

ISSN-e 2594-0317

An Efficient and Stable Electrochemical Sensor Based on PtPd/CZO (CuO-doped ZnO) Synergistically Modified Electrode for ppb-level Formaldehyde Detection

Siyu Chen[1], Li Jiang[1]*, Yahong Luo[2]*, Xiaowei Huang[1], Fan Zhang[1], Zhu Tao[1], Yanxia Liang[1], Jiao Liu[1]

[1]College of Materials and Chemistry, China Jiliang University, Hangzhou, 310018, People's Republic of China.
[2]School of Environment, Key Laboratory of Yellow River and Huai River Water Environment and Pollution Control, Ministry of Education, Henan Normal University, Xinxiang, 453007, People's Republic of China.

Abstract. An efficient formaldehyde (FA) detection system was developed through the functionalization of a glassy carbon electrode (GCE) with PtPd nanoparticles and CuO-doped ZnO (CZO) composite. A comprehensive suite of analytical techniques was employed to investigate the composite materials' morphology and electrocatalytic performance. The findings indicated that the bandgap energy and resistance value (R_{ct} + R_p) of PtPd/CZO nanoparticles (NPs) were 1.95 eV and 912.61 Ω, respectively, which are lower than those of CZO NPs. This indicates a higher surface electron transfer rate and enhanced catalytic properties for PtPd/CZO NPs. The electrocatalytic oxidation performance of the PtPd/CZO/GCE were thoroughly evaluated. The PtPd/Nafion/GCE sensor exhibited remarkable electrocatalytic performance toward formaldehyde electro-oxidation within a 0.1 M sulfuric acid medium, showing a linear response between 50.0 and 7000.0 μM along with a detection threshold of 5.8 μM. This sensor offers exceptional stability and reliability, with its practical application value proven through experiences.

J. Mex. Chem. Soc. **2026**, *70(1):e2490*
Regular Issue

ISSN-e 2594-0317

Resumen. Se desarrolló un sistema eficiente de detección de formaldehído (FA) mediante la funcionalización de un electrodo de carbono vítreo (ECV) con nanopartículas de PtPd y con un compuesto de ZnO (CZO) dopado con CuO. Se empleó un conjunto completo de técnicas analíticas para investigar la morfología y el rendimiento electrocatalítico de los materiales compuestos. Los resultados indicaron que la energía de banda prohibida y el valor de resistencia (Rct + Rp) de las nanopartículas (NP) de PtPd/CZO fueron de 1,95 eV y 912,61 Ω, respectivamente, inferiores a los de las NP de CZO. Esto indica una mayor tasa de transferencia de electrones en la superficie y mejores propiedades catalíticas para las NP de PtPd/CZO. Se evaluó exhaustivamente el rendimiento de la oxidación electrocatalítica en PtPd/CZO/ECV. El sensor PtPd/Nafion/GCE mostró un rendimiento electrocatalítico excepcional en la electrooxidación de formaldehído en un medio de ácido sulfúrico 0,1 M, con una respuesta lineal entre 50,0 y 7000,0 µM, y un umbral de detección de 5,8 µM. Este sensor ofrece una estabilidad y fiabilidad excepcionales, con un valor práctico comprobado por la experiencia.

Introduction

Formaldehyde (HCHO or FA), an invisible volatile organic compound (VOC) possessing a sharp, irritating smell, is universally recognized as a poisonous and cancer-causing agent [1,2]. FA has been identified as an unauthorized preservative in certain manufactured food products, primarily because of its antibacterial characteristics [3]. Excessive FA exposure has been associated with acute conditions including headaches [4], abdominal discomfort [5], and respiratory impairment [6], while chronic low-level exposure to FA may interfere with genomic DNA methylation patterns [7]. Formaldehyde (FA) contamination in potable water and food products has increasingly drawn scientific and regulatory concern, thereby establishing FA detection in liquid matrices as a critical priority across food safety and public health research domains [8-10].

Diverse analytical methods have been employed for quantitative FA detection, such as the colorimetric method [11], Chromatography methods [12] and fluorometric methods [13]. Due to issues with accuracy, equipment, and operating procedures, there is an urgent need for a fast and convenient method for on-site detection [14]. For direct electrochemical detection of formaldehyde (FA), various nanomaterials have been used as catalysts, including platinum, nickel-doped P (Ni/P) nanozeolite [15], Cu-codoped ZnO [16], and spinel zinc ferrite (ZnFe2O4) nanorods [17]. These materials demonstrate fast response times and excellent selectivity. In recent years, sensors based on ZnO/CuO heterostructure (CZO) have become a research hotspot [18, 19]. CuO and ZnO can form stable p-n heterostructures owing to their well-matched band structures and the carrier differences between them. Yoo et al. [20] prepared flower-like CuO-ZnO heterogeneous structure gas sensor using the hydrothermal method. Experimental results demonstrated a reduced response time and improved detection sensitivity. Mariammal et al. [21] synthesized ZnO-CuO sensor by co-precipitation method, which has good sensing performance for ethanol. Diltemiz et al. [22] employed electrospinning to fabricate CuO-ZnO composite nanofibers that served as sensitive layers for quartz crystal microbalance sensors. Operating at ambient temperature, the resulting device exhibited a limit of detection of 41.0 ppb and exhibited a linear sensitivity of 0.11 Hz per ppb across the concentration range 0.5 to 50.0 ppm. The sensors responded within 80.0 s and displayed excellent selectivity toward formaldehyde over common interfering volatile organic compounds.

Dual-metal nanomaterials, composed of two different metallic elements, allow for precise adjustment of their dimensions, elemental makeup, and structural form. This tailored approach improves performance and broadens application scope across energy storage systems, optical detection mechanisms, and chemical analysis techniques [23]. Especially noteworthy is the superior catalytic performance demonstrated by dual-metal nanomaterials relative to their single-metal counterparts, thereby identifying them as valuable candidates for advanced catalytic systems [24]. Nguyen et al. [25] reported the development of combined-metal PtPd@ZnO core-shell nanoparticles (CSNPs) using a hydrothermal method. Computational DFT analyses demonstrated that the blended PtPd core possesses remarkable inherent hydrogen adsorption capacity, outperforming both standalone Pd and the ZnO shell. Cai et al. [26] developed

http://dx.doi.org/10.29356/jmcs.v70i1.2490

J. Mex. Chem. Soc. **2026**, *70(1):e2490*
Regular Issue

ISSN-e 2594-0317

a hydrogen detection device on a patterned sapphire substrate (PSS) that demonstrates superior sensitivity compared to pure palladium (Pd) sensors and broadens the detection range to 100 % hydrogen concentration. Zhao et al. [27] reported the synthesis of mesoporous cubic Pd, Pt, and PdxPt (x = 0.43~8.52) alloys via the KIT-6 templating strategy for methane oxidation. Pt doping notably adjusted the redox properties of Pd, and the Pt–Pd oxide demonstrated superior catalytic performance and thermal stability compared to the metallic material. Wu et al. [28] optimized this synergistic effect by adjusting the Co/Pd ratio during the synthesis of Co/Pd nanoparticles, reaching the maximum near Co0.24Pd0.76, enabling complete cobalt transformation under the most moderate thermal conditions.

Platinum (Pt) nanoparticles demonstrate catalytic properties toward numerous chemical substances, with their effectiveness enhanced through particle shape optimization and metal alloying strategies that leverage structural design principles and cooperative interactions [29]. Adding palladium (Pd) as a second metal improves the electrode's catalytic oxidation efficiency for formaldehyde. Without palladium, water dehydrogenation on platinum requires a higher electrical potential (over 0.5 V), as demonstrated in studies on hydrogen evolution reaction (HER) mechanisms [30]. Specifically, platinum is known to be an efficient electrocatalyst for water reduction, but its practical applications are often limited by the high overpotential required for the reaction [31]. In contrast, the introduction of palladium can significantly lower this overpotential, enhancing the catalytic efficiency [32]. Therefore, a synergistic effect between Pt and Pd nanoparticles (NPs). The incorporation of PtPd alloy catalysts introduces a bimetallic synergy that optimizes the electronic structure, significantly enhancing catalytic activity [33].

This research presents an innovative method for functionalizing glassy carbon electrodes (GCE) with PtPd and CZO nanomaterials, resulting in the PtPd/CZO/GCE composite structure. The innovation of this work lies in the strategic combination of PtPd and CZO nanoparticles, which optimizes the electrode's performance. The electrocatalytic oxidation performance of the PtPd/CZO/GCE were thoroughly evaluated and its practical application value has been proven. This research can also contribute to the cultivation of top-notch newengineering talents with excellent innovative literacy.

Experimental

Synthesis of CZO NPs

50.0 mL 0.1 M CuCl2 solution and 50.0 mL 0.1 M ZnCl2 solution were mixed in a 250.0 mL conical flask, heating at 50.0 ℃ and stirring continuously for 0.5 hour until disperse completely. After adding 100.0 ml 0.1 M NH4OH solution into the mixture, the water bath temperature was adjusted to 75.0 ℃ stirring for 5.0 hours continuously. During the reaction mixture's cooling process, a cyan-colored CZO nanoparticle precipitate appeared. This precipitate underwent washing with deionized water and anhydrous ethanol, followed by high-speed centrifugation. The precipitate was dried at room temperature for 0.5 hour and subsequently heated in an oven at 52.0 ℃ for 3.0 hours. The CZO NPs were thus prepared for further experiments and characterizations.

Fabrication of the PtPd/CZO/GCE electrode material

GCEs (4.0 mm diameter) were polished to a mirror-like surface using 0.5 μm aluminum oxide suspension on a polishing apparatus, followed by ultrasonic cleaning in anhydrous ethanol and deionized water for 5.0 minutes each [34]. Following nitrogen drying, the electrode underwent activation through immersion in 0.1 M sulfuric acid solution, with cyclic voltammetry (CV) conducted at a 100.0 mV/s scan rate across the -1.0 to 1.0 V potential window. 20.0 mL 0.5 wt.% Nafion solution was mixed with the CZO NPs and then vibrated rapidly on the oscillator for 10.0 min, followed by ultrasound for 20.0 minutes. Later, 6.0 μL of the mixed substance was transferred onto the spotless glassy carbon electrode (GCE) surface, drying in the air to obtain the CZO/GCE.

PtPd NPs were electrodeposited on the surface of CZO/GCE from a bath containing 0.001 M H2PtC16, 0.001 M PdCl2 and 0.1 M H2SO4 in cyclic voltammetry mode for 40.0 turns at a scan rate of 50.0 mV/s, from -0.3 V to 0.3 V. Upon completion of the modification process, the electrode was removed and thoroughly rinsed with deionized water, resulting in the PtPd/CZO/GCE sensor.

http://dx.doi.org/10.29356/jmcs.v70i1.2490

J. Mex. Chem. Soc. **2026**, *70(1):e2490*
Regular Issue

ISSN-e 2594-0317

An analogous method was employed to fabricate PtPd/GCE and bare GCE electrodes for comparative analysis. During the electrode preparation and throughout the experimental process, no significant flaking or detachment was observed on the electrode surface. The dissolution of effective substances has not been taken into account in similar related studies either [35,36]. Therefore, we can consider that the dissolution of ZnO can be disregarded. A diagram depicting the PtPd/CZO/GCE fabrication procedure is presented in Fig. 1.

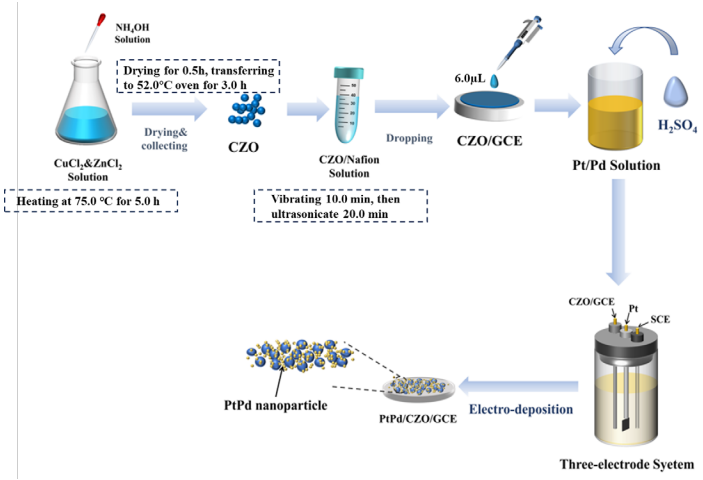

Fig. 1. Schematic of the PtPd/CZO /GCE fabrication.

Characterization

The material's microstructural characteristics and surface morphology were analyzed via scanning electron microscopy (SEM, ZEISS-SUPRA55). The element distribution within CZO NPs and PtPd/CZO NPs was recorded via Energy dispersive spectroscopy (EDS, Oxford EDS 7426). The binding energies of elements were determined through X-ray photoelectron spectroscopy (Thermo ESCALAB 250 XPS system). Sample crystallographic structures were characterized via X-ray diffraction analysis (Rigaku Ultima IV XRD system). An aluminum target operating at 1486.6 eV served as the excitation source for these analyses. The Ar^+ sputtering beam had an energy of 2000.0 eV and an incidence angle of 58°. CZO NPs and PtPd/CZO NPs were explored with the UV diffuse reflectance spectra (Evolution 300 ultraviolet-visible spectrophotometer. The wavelength range is 190.0 – 1100.0 nm, with a Smart NIR integrating sphere attachment for diffuse reflection measurement, Thermo Scientific). For UV-Vis diffuse reflectance spectroscopy (DRS), the nanoparticles were suspended in deionized water. The structural characteristics of PtPd/CZO nanoparticles were examined via field-emission scanning electron microscopy (FESEM) using the Zeiss LIBRA 200FE model from Germany. All electrochemical measurements were performed with CHI 660e potentiostat systems under ambient temperature conditions.

Electrochemical analyses, comprising Electrochemical Impedance Spectroscopy (EIS), Cyclic Voltammetry (CV), Linear Sweep Voltammetry (LSV) curves, and current-time (i-t) curves, were performed within a standard three-electrode cell configuration. The electrochemical cell configuration consisted of a PtPd/Nafion/GCE working electrode, a saturated calomel reference electrode (KCl-sat.), and a platinum foil counter electrode. All experimental procedures were carried out in an electrolyte solution of 0.1 M sulfuric acid containing 5.0 mM formaldehyde (FA). The analytical performance of the PtPd/Nafion/GCE-based FA sensor was assessed utilizing cyclic voltammetry (CV), linear sweep voltammetry (LSV), and current-time (i-t) curve data.

J. Mex. Chem. Soc. **2026**, *70(1):e2490*
Regular Issue

ISSN-e 2594-0317

Results and discussion

Characterization of the PtPd/CZO NPs

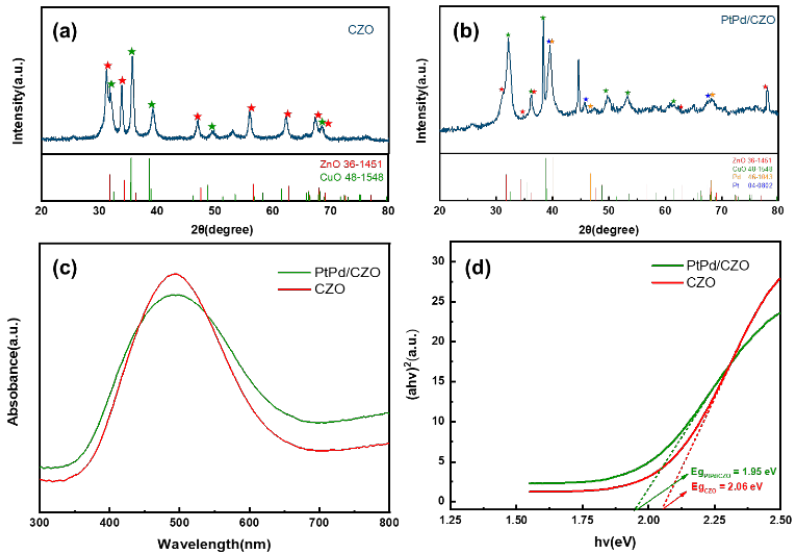

Fig. 2. (a,b) XRD spectra of CZO and PtPd/CZO NPs ; and spectroscopic characterization of CZO NPs and PtPd/CZO NPs: **(c)** UV-Vis DRS, **(d)** Tauc's plot for the E_g estimation.

Fig. 2**(a)** shows the XRD spectra of the CZO NPs, which exhibit prominent peaks corresponding to CuO (JCPDS 48-1548) and ZnO (JCPDS 36-1451), confirming the presence of CuO and ZnO in the CZO NPs. Fig. 2**(b)** presents the XRD spectra of PtPd/CZO, where similar peaks to those in Fig. 2**(a)** can be observed. Notably, a sharp peak appears around 39.98°, corresponding to Pt (JCPDS 04-0802) and Pd (JCPDS 46-1043). These XRD peaks confirm that PtPd NPs were successfully electrodeposited onto the surface of the CZO NPs. Furthermore, all the peaks in the XRD spectra are sharp, indicating that both the CZO NPs and the PtPd/CZO NPs exhibit high crystallinity. Comparing Fig. 2**(a)** and Fig. 2**(b)**, it is observed that the peak corresponding to ZnO at approximately 31.72° decreases, indicating a reduction in the Zn content in the PtPd/CZO NPs, as further confirmed by the subsequent EDS analysis (Fig. 3(**A**)). This decrease is attributed to the presence of H_2SO_4 in the electrodeposition solution, which coupled with the amphoteric nature of ZnO causes the partial dissolution of ZnO [37].

The UV diffuse reflectance spectra (UV-Vis DRS) for the CZO NPs and PtPd/CZO NPs were shown in Fig. 3**(A)**(c). The UV-Vis DRS of the CZO NPs (pink) and PtPd/CZO NPs (green) were recorded between 300.0 nm and 800.0 nm. There is a peak at around 503.0 nm in both two plots. The bandgap energy (E_g) of the PtPd/CZO and the CZO were estimated according to Tauc's Eq. (i) by applying UV-Vis DRS data [38,39]. As shown in Fig. 3**(A)**(d), the E_g of CZO NPs and PtPd/CZO NPs are 2.06eV and 1.95eV respectively. PtPd NPs exhibit a synergistic catalytic effect, which can reduce the bandgap and enhance their catalytic properties [40]. A smaller band gap enhances the generation efficiency of photogenerated electron-hole pairs, reduces the activation energy for catalytic reactions, improves catalyst conductivity, and increases resistance to CO poisoning. This enables more electrons to participate in the catalytic process, thereby boosting overall catalytic performance [41,42].

http://dx.doi.org/10.29356/jmcs.v70i1.2490

J. Mex. Chem. Soc. **2026**, *70(1):e2490*
Regular Issue

ISSN-e 2594-0317

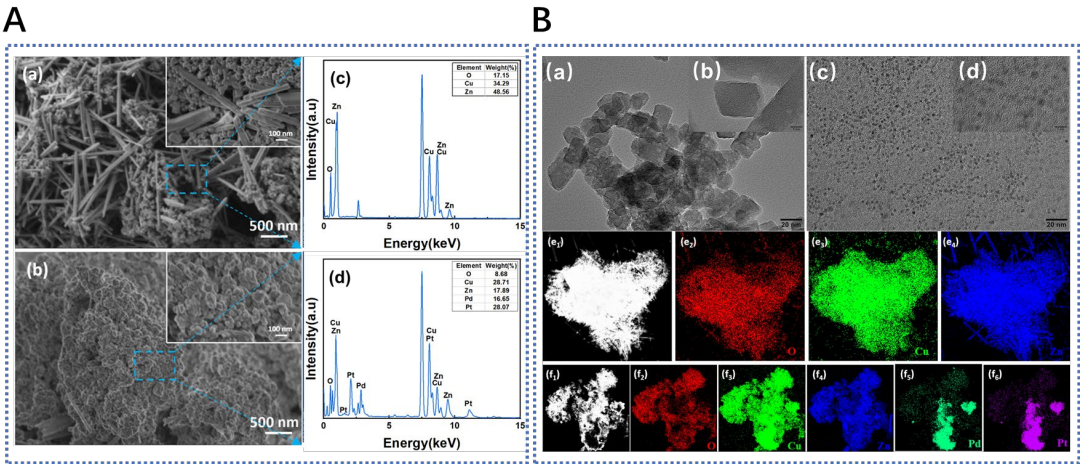

Fig. 3. (A) (a,b) Morphology and (c,d) elemental analysis of CZO NPs and PtPd/CZO NPs. **(B)** TEM images of (a,b) CZO NPs, (d,e) PtPd/CZO NPs. EDS images of (e1-e4) O, Cu and Zn on CZO NPs and (f1-f6) O, Cu, Zn, Pt and Pd on PtPd/CZO NPs.

Surface morphology and elemental composition of CZO NPs and PtPd/CZO NPs were analyzed through scanning electron microscopy (SEM) and energy-dispersive X-ray spectroscopy (EDS), with results presented in Fig. 3**(A)** and **(B)**. CZO NPs cover the GCE, serving as a porous carrier, while PtPd NPs are well-distributed on the CZO NPs' surface, as seen in the mapping image. Comparing the EDX data in Fig. 3**(B)** (e2, e3, and f3) reveals a decrease in Zn content in PtPd/CZO NPs, consistent with the XRD analysis results.

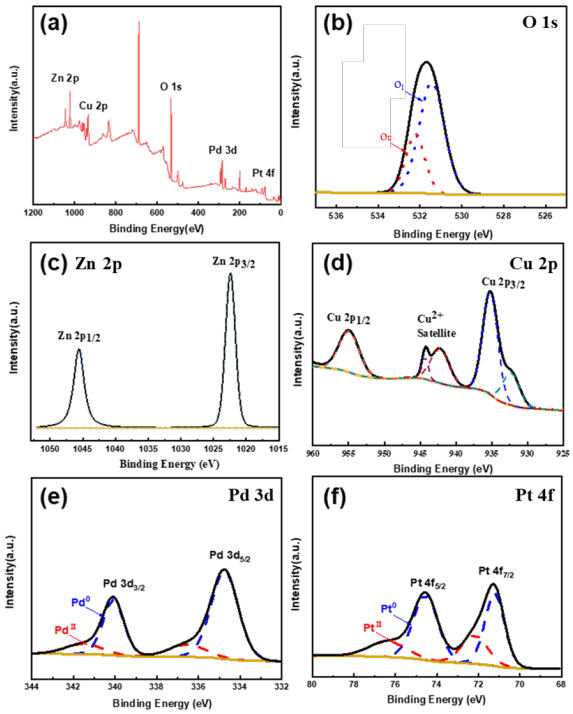

Fig. 4. (a)XPS survey spectra of PtPd/CZO/GCE; **(b-f)** XPS fine spectra of O 1s, Cu 2p, Zn 2p, Pd 3d and Pt 4f on PtPd/CZO/GCE.

http://dx.doi.org/10.29356/jmcs.v70i1.2490

J. Mex. Chem. Soc. **2026**, *70(1):e2490*
Regular Issue

ISSN-e 2594-0317

The XPS spectra of PtPd/CZO NPs are presented in Fig. 4. From the full XPS spectrum of PtPd/CZO NPs (Fig. 4**(a)**), it is evident that the PtPd/CZO NPs are composed of Cu, Zn, O, Pt and Pd elements. Fig. 4**(b-f)** display the high-resolution scanning spectra of the O1s, Cu2p, Zn2p, Pd3d, and Pt4f orbitals, respectively. In Fig. 4**(b)**, O1s spectrum can be deconvoluted into two peaks. O_I corresponds to O^{2-} ions in the crystal, while O_{II} represents oxygen vacancies in the crystal or O^- and O^{2-} ions in oxygen defects. Fig. 4**(c)** displays the distinctive Zn 2p3/2 and Zn 2p1/2 spectral lines of ZnO, which correspond to binding energies of 1021.78 eV and 1044.86 eV respectively. The energy difference between the two Zn 2ps peaks is 23.08 eV, indicating the presence of Zn^{2+}. From the narrow spectrum of Fig. 4**(d)**, satellite peaks are observed between 942.0 and 944.0 eV with two characteristic peaks at 932.18 eV on the left and 951.98 eV on the right. These peaks are attributed to the Cu $2p_{3/2}$ and Cu $2p_{1/2}$ states, respectively. The energy difference between these two binding energies is 19.80 eV, which indicates the presence of Cu^{2+}. Therefore, it can be concluded that both ZnO and CuO are present in PtPd/CZO [43]. Fig. 4**(f)** shows the high-resolution Pt 4f, which displays two obvious peaks. These peaks can be further deconvoluted into Pt (0) at 70.18 eV and 73.58 eV, and Pt (II) at 71.68 eV and 75.28 eV. In Fig. 4**(e)**, the two main peaks of Pd 3d can also be deconvoluted into two pairs of peaks. The peaks at 334.68 eV and 339.98 eV correspond to the presence of metallic Pd (0), while the peaks at 335.78 eV and 341.17 eV are associated with the oxidized form of Pd(II), such as PdO and $Pd(OH)_2$.

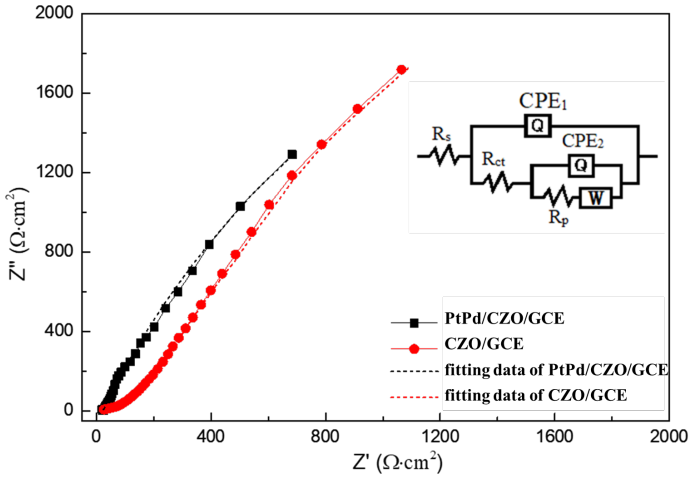

Fig. 5. Nyquist plots and equivalent circuits of the EIS for CZO/GCE and PtPd/CZO/GCE in 0.1 M H_2SO_4 containing 5mM FA. Sequential lines represent the fits using equivalent circuits.

Table 1. Fitting results of EIS plots for CZO/GCE and PtPb/CZO/GCE in 0.1 M H2SO4 containing.

Sample	R_s/Ω	CPE_1/μF	n_1	R_{ct}/Ω	CPE_2/μF	n_2	R_p/Ω	W/ S-sec$^{0.5}$	(R_{ct} + R_p)
CZO	4.913	50.32	0.800	74.61	229.2	0.789	1187.50	31.28	1262.11
PtPdCZO	5.559	48.04	0.800	23.41	113.8	0.794	889.20	10.19	912.61

Electrochemical impedance spectroscopy (EIS) is an effective method for assessing resistance. The charge transfer resistance (R_{ct}) and film resistance (R_p)of PtPb/CZO/GCE are investigated. The resistance value (R_{ct} + R_p) of CZO films is 1262.11 Ω, while that of the PtPd/CZO film is 912.61 Ω. This indicates that PtPd/CZO/GCE has higher surface electron transfer rate, which enhances the electrocatalytic efficiency.

http://dx.doi.org/10.29356/jmcs.v70i1.2490

J. Mex. Chem. Soc. **2026**, *70(1):e2490*
Regular Issue

ISSN-e 2594-0317

Electrocatalytic oxidation of PtPb/CZO/GCE toward FA

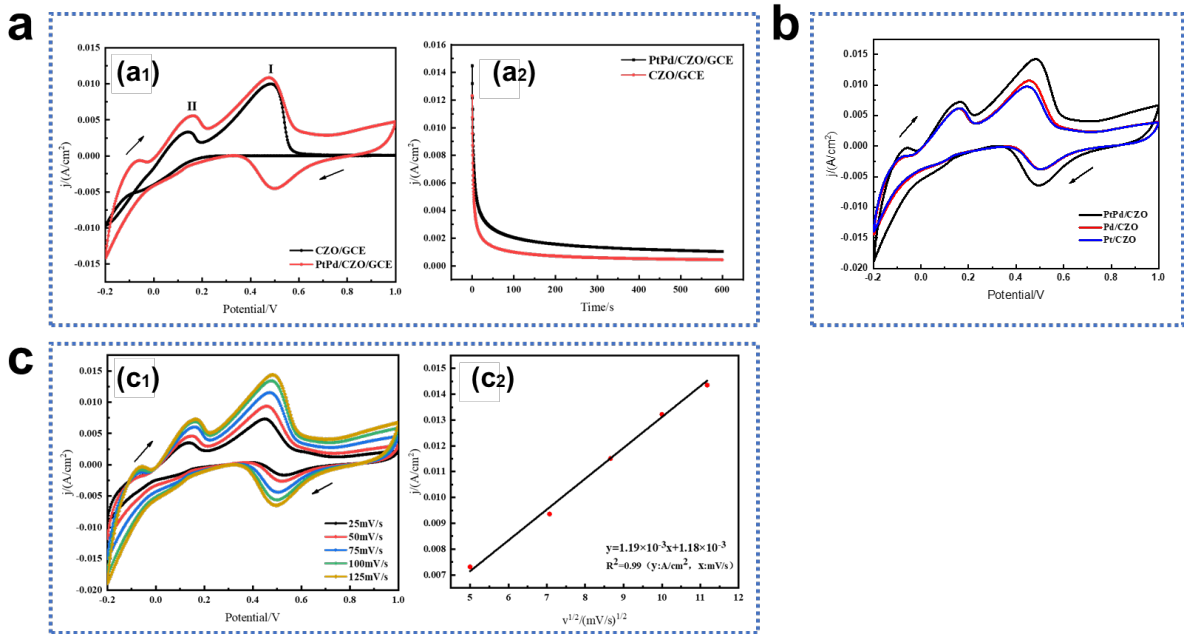

Fig. 6. (a) (a_1) CV curves and (a_2) i-t curves of PtPd/CZO/GCE and CZO/GCE in 0.1 M H2SO4 containing 5.0 mM FA. **(b)** CV curves of Pd/CZO/GCE, Pt/CZO/GCE and PtPd/CZO/GCE (scan rate: 100.0 mV/s). **(c)**(c_1) Effect of scan rate on CV curves of PtPd/CZO/GCE in 0.1 M H_2SO_4 containing 5.0 mM FA; (c_2) the relationship between $v^{1/2}$ and oxidation peak current density

Fig. 6**(a)**a_1 shows the CV curves of CZO/GCE and PtPd/CZO/GCE in 0.1 M H_2SO_4 containing 5.0 mM FA. CZO/GCE exhibits a strong response to formaldehyde oxidation, with two distinct and reproducible oxidation peaks at 0.5 V (peak I) and 0.2 V (peak II). The current density of oxidation peak I is the highest, reaching approximately 9.78 mA/cm^2, indicating effective catalytic oxidation of formaldehyde. After modification with PtPd, the current density of oxidation peak I increases to 10.98 mA/cm^2, suggesting enhanced catalytic performance. The oxidation reaction of formaldehyde on the CZO/GCE surface can be expressed as follows:

$$HCHO+H_2O \rightarrow HCOOH+2H^+ +2e^- \quad \text{(eq.1)}$$

$$HCHO+H_2O \rightarrow CO_2+4H^+ +4e^- \quad \text{(eq.2)}$$

The formaldehyde oxidation peaks I and II correspond to the equations 1 and 2, respectively. During the positive scan of PtPd/CZO/GCE, a small oxidation peak appears around -0.1 V, which is likely associated with a hydrogen adsorption reaction. During the cathodic scan, a prominent reduction peak appears at approximately 0.5 V, signaling the reduction of PtPd oxide species. According to the Randles-Sevcik equation [44], Comparing to CZO/GCE, the PtPd/CZO/GCE electrode exhibits roughly 1.2 times the effective electroactive surface area. This enhancement in formaldehyde response performance is attributed to the synergistic effect of PtPd, which improves the catalytic activity of PtPd/CZO/GCE. Fig. 6**(a)**a_2 shows that CZO/GCE and PtPd/CZO/GCE exhibit a large response current to formaldehyde. Their catalytic activities decrease rapidly during the first 100.0 s, then gradually stabilize. However, the performance of PtPd/CZO/GCE remains consistently superior to that of CZO/GCE throughout the process.

http://dx.doi.org/10.29356/jmcs.v70i1.2490

J. Mex. Chem. Soc. **2026**, *70(1):e2490*
Regular Issue

ISSN-e 2594-0317

The fabricated CZO/GCE and PtPd/CZO/GCE both exhibit reversible peaks, as shown in Fig. 6**(b)**. The PtPd/CZO@GCE generates measurable and reproducible redox peaks at a scan rate of 100 mV/s, indicating its superior electrocatalytic properties for HCHO molecules [45]. This observation confirms that PtPd/CZO NPs exhibit electrocatalytic properties similar to those of Pd/CZO NPs or Pt/CZO NPs, consistent with the findings discussed earlier.

The cyclic voltammogram in Fig. 6**(c)** demonstrates characteristics of a quasi-reversible process. This is evident from the shape of the peaks, which are not perfectly symmetrical but exhibit slight distortions. The peak currents increase with the square root of the scan rate, as shown by the multiple curves at different scan rates (25.0, 50.0, 75.0, 100.0, and 125.0 mV/s), suggesting that the process is not fully reversible but is influenced by diffusion. The influence of scan rate (ν) on the electrocatalytic oxidation of formaldehyde at the PtPd/CZO/GCE was systematically investigated. As shown in Fig. 6**(c)**, within the range 25.0 ~125.0 mV $\cdot$ s^{-1} the anodic peak current density exhibits a linear correlation with $\nu^{1/2}$ ($R^2 = 0.99$), in accordance with the Randles–Sevcik equation for a diffusion-controlled process. Concomitantly, the peak potential shifts positively with increasing scan rate, consistent with quasi-reversible kinetics. Based on these results, a scan rate of 100.0 mV$\cdot$ s^{-1} was selected as the optimal detection condition: it delivers a sufficiently large j_{peak} while minimizing capacitive background, and further increases in ν yield only marginal gains in current density.

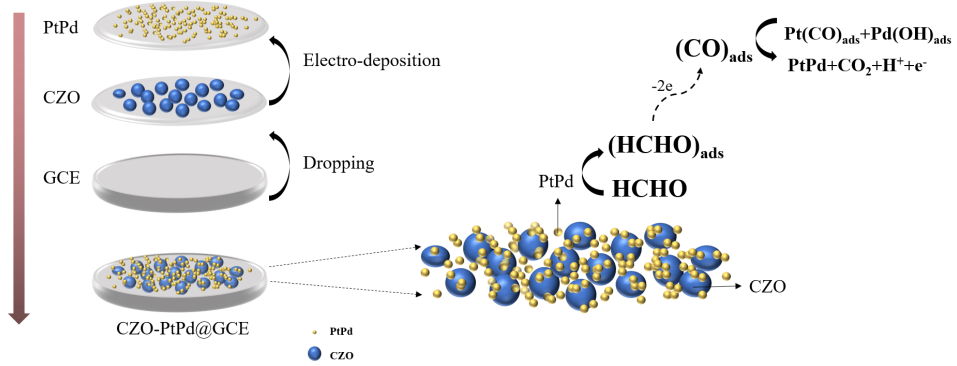

Fig. 7. Oxidation mechanism of formaldehyde on PtPd/CZO/GCE in H_2SO_4 solution

Under acidic conditions, the oxidation of formaldehyde at the modified electrode predominantly occurs via the formation of adsorbed carbon monoxide (CO) molecules on the catalyst surface ((CO)ads), which serves as the primary toxic intermediate in the catalytic oxidation process. A good formaldehyde catalyst should demonstrate excellent oxidation capacity for $(CO)_{ads}$. Fig. 7 illustrates the oxidation mechanism of formaldehyde on CZO/GCE, which follows a simple oxidation reaction involving the transfer of two electrons and two protons. HCOOH generated during the reaction will be adsorbed onto the CZO/GCE surface, and toxic intermediates, such as $(CO)_{ads}$, will form in subsequent reaction, covering the active sites on the electrode surface. This results in the direct oxidation of formaldehyde to CO_2. The redox process of formaldehyde on the CZO/GCE surface is irreversible. CZO/GCE exhibits a better response to formaldehyde, showing a lower oxidation peak initial potential and higher peak current density. This enhanced performance may be attributed to the influence of the p-n heterojunction [46], which increases the active sites on the electrode surface and accelerates the electron migration rate. The oxidation performance of PtPd/CZO/GCE towards formaldehyde is better.

http://dx.doi.org/10.29356/jmcs.v70i1.2490

J. Mex. Chem. Soc. **2026**, *70(1):e2490*
Regular Issue

ISSN-e 2594-0317

Performance testing of FA sensors

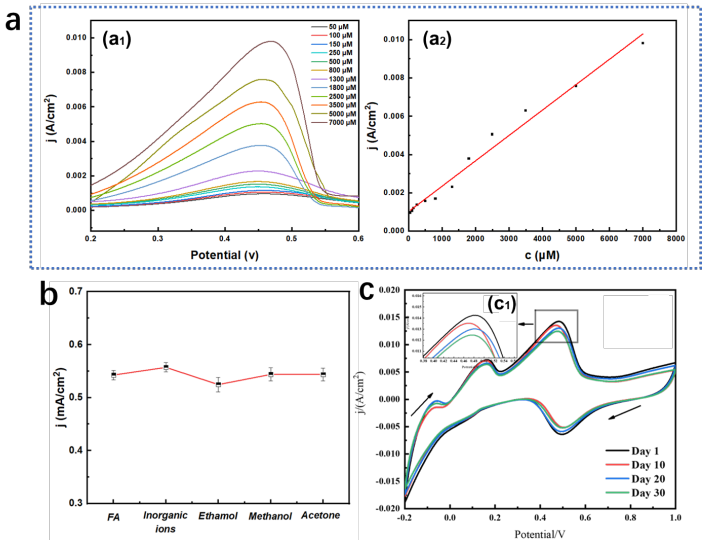

Fig. 8. (a) (a_1) Linear sweep voltammetry profiles recorded at the PtPd/CZO/GCE electrode in 0.1 M sulfuric acid across various formaldehyde concentrations; (a_2) calibration curve for the PtPd/CZO/GCE system, **(b)**Changes in i_p after the addition of different interfering substances, **(c)** CV curves of PtPd/CZO/GCE for FA at different times in 0.1 M H_2SO_4 containing 5 mM FA.

Quantitative assessment can be efficiently executed through the calibration curve approach, enabling analyte concentrations to be precisely quantified using a carefully prepared standard graph. The standard curve for PtPd/CZO/GCE, obtained through linear fitting using the least squares method, is shown in Fig. 8(a). The linear sweep voltammetry (LSV) was used to test PtPd/CZO/GCE with standard formaldehyde solutions of varying concentrations.

The LSV technique demonstrated quick and sensitive detection of FA, featuring a clear oxidation peak near 0.45 V. Within 0.1 M sulfuric acid, FA's oxidation peak current density correlated strongly with its concentration, ranging from 5.0×10^{-5} to 7.0×10^{-3} mol/L. The linear regression equation appears below, with the corresponding limit of detection (LOD) computed as 5.8×10^{-6} mol/L via eq. 3.

$$J = 0.01024 + 1.32521\times10^{-5}\times C,\ R^2 = 0.983\ (j\text{: A/cm}^2,\ C\text{: mol/L}) \qquad \text{(eq.3)}$$

Compared with the PtPd/Nafion/GCE sensor [47], the PtPd/CZO/GCE sensor exhibits a significantly broader linear range, extending to concentrations exceeding 5000.0 μM. This enhanced range is complemented by superior selectivity for formaldehyde, thereby effectively mitigating the impact of potential interfering substances. Relative to SnO_2-based sensors [48], the PtPd/CZO/GCE sensor achieves a stable response more rapidly, highlighting its efficiency in dynamic sensing environments. When juxtaposed against several formaldehyde (FA) sensors with detection limits ranging from 1.63 to 100.0 μM, the PtPd/CZO/GCE sensor demonstrates markedly enhanced performance. The synergistic interplay between Pt and Pd within the PtPd/CZO/GCE framework significantly augments the sensor's electrocatalytic activity and stability. These improvements collectively bolster the sensor's resistance to interference and ensure consistent repeatability across multiple measurements, thus positioning it as a highly reliable tool for formaldehyde detection.

Assessments of the PtPd/CZO/GCE sensor's reproducibility and stability were conducted. Selectivity evaluations involved introducing various ions and molecules (Na^+, K^+, Ca^{2+}, Cl^-, CO_3^{2-}, NO_3^-,

http://dx.doi.org/10.29356/jmcs.v70i1.2490

J. Mex. Chem. Soc. **2026**, *70(1):e2490*
Regular Issue

ISSN-e 2594-0317

acetone, methanol, ethanol) separately into a 0.1 M sulfuric acid solution with 5 mM FA, with selectivity assessment performed via linear sweep voltammetry (LSV). Fig. 8(b) illustrates the variations in peak current (i_p) following the introduction of various interfering substances. Findings reveal that 50.0 mM concentrations of inorganic ions produce negligible effects on the current response. Even at 25.0 mM concentrations of methanol and ethanol, the relative error for peak FA oxidation current density stayed under 5.0%. These results confirm the superior selectivity of the PtPd/CZO/GCE sensor for formaldehyde detection.

The PtPd/CZO/GCE sensor's durability was evaluated by tracking FA electrocatalytic oxidation at ambient conditions on days 1.0, 10.0, 20.0, and 30.0, with results presented in Fig. 8(c). The oxidation peak current density (i_p) near 0.49 V showed remarkable consistency, ranging from 13.94 to 14.26 mA/cm^2 throughout the 30-days period. Specifically, ip values decreased minimally from 5.18 mA/cm^2 initially to 5.02 mA/cm^2 after 30.0 days, representing just a 2.3 % performance decline. These findings confirm that the PtPd/CZO/GCE sensor preserves its effectiveness for over a month, demonstrating exceptional long-term reliability and suitability for real-world FA detection scenarios.

The PtPd/CZO/GCE sensor, utilizing the LSV method, was employed to evaluate the water quality of the school's artificial lake. The standard addition method was implemented to assess recovery rates of added standards, with triplicate experiments conducted to ensure data accuracy. Recovery values ranged from 97.7% to 103.4 %, accompanied by an RSD (n=3.0) below 3.9 %. These results demonstrate the sensor's consistent performance and high dependability. Consequently, the PtPd/CZO/GCE sensor proves suitable for meeting routine formaldehyde detection requirements in real water samples.

To validate the formaldehyde concentrations obtained from the LSV analysis of the school's artificial lake water, a second analytical technique, HPLC-UV (High-Performance Liquid Chromatography with Ultraviolet Detection) was employed. This method is widely recognized for its accuracy and reliability in quantifying formaldehyde in complex matrices. The HPLC-UV analysis was conducted using a C18 column with a mobile phase of acetonitrile and water (gradient elution), and detection was performed at 240.0 nm. The results from HPLC-UV were in excellent agreement with those from LSV, confirming the reliability of the electrochemical method for formaldehyde detection in real water samples [49-51].

The PtPd/CZO/GCE sensor demonstrates high selectivity for formaldehyde detection, with minimal interference from potential interferents like cations, methanol, and ethanol. Key evidence includes the distinct oxidation potentials of formic acid and acetaldehyde compared to formaldehyde, which facilitates selective detection without significant electrochemical overlap. This aligns with Diltemiz et al.'s [22] findings that CuO-ZnO nanofibers can selectively detect formaldehyde amidst methanol and ethanol, affirming the negligible impact of formic acid and acetaldehyde under optimized conditions. Thus, the sensor's design is effective for precise formaldehyde detection, corroborated by consistent electrochemical system performance and literature precedent [52].

Conclusions

(1) This research presents an innovative method for jointly functionalizing glassy carbon electrodes (GCE) with PtPd and CuO-doped ZnO (CZO) nanoparticles, yielding the PtPd/CZO/GCE composite material. This method strategically combined PtPd and CZO nanoparticles to optimize the overall performance of the electrode.

(2) The electrocatalytic oxidation performance of the PtPd/CZO/GCE were thoroughly evaluated. The bandgap energy and resistance value (R_{ct} + R_p) of PtPd/CZO nanoparticles (NPs) were 1.95 eV and 912.61 Ω, respectively, which are lower than those of CZO NPs. This indicates a higher surface electron transfer rate and enhanced catalytic properties for PtPd/CZO NPs.

(3) Within 0.1 M sulfuric acid medium, FA's oxidation peak current density exhibited a robust linear correlation across concentrations ranging from 50.0 to 7000.0 μM, with a detection threshold of 5.8 μM. This sensing system further exhibited outstanding durability and dependability, rendering it appropriate for routine formaldehyde monitoring in aquatic settings.

http://dx.doi.org/10.29356/jmcs.v70i1.2490

ISSN-e 2594-0317

Acknowledgements

This work was supported by the Basic Public Welfare Research Program of Zhejiang Province (Grant No. LGG22E010002) and 2022 Zhejiang Province Curriculum-based Ideological and Political Education Project (Document No. ZJED [2022] 51, Project No. 117).

References

1. Silva, A. M.; Castelo-Branco, I. M.; Quinta-Ferreira, R. M.; Levec, J. *Chem.Eng. Sci.* **2003**, *58*, 963-970. DOI: https://doi.org/10.1016/S0009-2509(02)00636-X
2. Swenberg, J. A.; Moeller, B. C.; Lu, K.; Rager, J. E.; Fry, R. C.; Starr, T. B. *Toxicol.Pathol.* **2013,** *41*, 181-189.
3. Malakhova, N.; Mozharovskaia, P.; Kifle, A. B.; Kozitsina, A. *Anal. Methods.* **2022,** *14*, 3423-3433.
4. Kurth, T.; Holtmann, G.; Neufang-Hüber, J.; Gerken, G.; Diener, H. J. *Cephalalgia.* **2006,** *26*, 506-510. DOI: https://doi.org/10.1111/j.1468-2982.2005.01076.x
5. Mavromichalis, I. *J. Pediatr. Gastroenterol. Nutr.* **1997**, *24*, 365,366. DOI: https://doi.org/10.1097/00005176-199703000-00026
6. Hwang, H.-S.; Choi, H.-S.; Bin, J.-H.; Kim, Y.-H.; Lee, I.-G.; Chung, S.-Y. *Journal of the Korean Child Neurology Society.* **2008**, 169-174.
7. Liu, Q.; Yang, L.; Gong, C.; Tao, G.; Huang, H.; Liu, J.; Zhang, H.; Wu, D.; Xia, B.; Hu, G. *Toxicol. Lett* **2011**, *205*, 235-240. DOI: https://doi.org/10.1016/j.toxlet.2011.05.1039
8. Vellingiri, K.; Deep, A.; Kim, K.-H.; Boukhvalov, D. W.; Kumar, P.; Yao, Q. J. S. *Sensors Actuators B: Chem.* **2017,** *241*, 938-948. DOI: https://doi.org/10.1016/j.snb.2016.11.017
9. E. F. S. A. J. E. *EFSA J.* **2011**, *9*, 2097. DOI: https://doi.org/10.2903/j.efsa.2011.2097
10. Chu, Z.-X.; Song, Q.; Zhang, Y.-Q.; Jiang, J. *Coord. Chem. Rev.* **2023**, *495*, 215338. DOI: https://doi.org/10.1016/j.ccr.2023.215338
11. Ai, J.; Cui, Y.; Ren, M.; Liu, K.; Wang, S.; Wu, Q.; Wang, X.; Kong, F. J. *Microchem. J.* **2024**, 110902. DOI: https://doi.org/10.1016/j.microc.2024.110902
12. Wang, Z.; Li, M.; Xu, S.; Sun, L.; Li, L. J. *Anal. Chim. Acta.* **2024**, *1318*, 342905.
13. Roy, S.; Pan, S.; Choudhury, N.; Sivaram, S.; De, P. *Eur. Polym. J.* **2024**, 113241. DOI: https://doi.org/10.1016/j.eurpolymj.2024.113241
14. Gibson, L.; Kerr, W.; Nordon, A.; Reglinski, J.; Robertson, C.; Turnbull, L.; Watt, C.; Cheung, A.; Johnstone, W. *Anal. Chim. Acta.* **2008**, *623*, 109-116. DOI: https://doi.org/10.1016/j.aca.2008.06.002
15. Azizi, S. N.; Ghasemi, S.; Amiripour, F. J. S. *Sensors Actuators B: Chem.* **2016,** *227*, 1-10. DOI: https://doi.org/10.1016/j.snb.2015.11.142
16. Ganesh, V. J. *Opt. Mater.* **2022,** *132*, 112834. DOI: http://dx.doi.org/10.1016/j.optmat.2022.112834
17. Vinosha, P. A.; Mely, L. A.; Jeronsia, J. E.; Krishnan, S.; Das, S. J. *Optik.* **2017,** *134*, 99-108. DOI: https://doi.org/10.1016/j.ijleo.2017.01.018
18. Liu, J.; Chen, Y.; Zhang, H. *Sensors Actuators B: Chem.* **2021,** *21*, 4685. DOI: https://doi.org/10.3390/s21144685
19. Li, S.; Yu, L.; Zhang, C.; Li, X.; Cao, L.; Du, H.; Fan, X. *Sensors Actuators B: Chem.* **2024**, 136179. DOI: https://doi.org/10.1016/j.snb.2024.136179
20. Yang, Y.; Kim, S.; Kim, K.; Jung, D. G.; Jung, D. *Surf. Interfaces.* **2024,** *46*, 104131. DOI: https://doi.org/10.1016/j.surfin.2024.104131
21. Mariammal, R.; Ramachandran, K. J. *Mater. Res. Bull.* **2018,** *100*, 420-428.DOI: https://doi.org/10.1016/j.materresbull.2017.12.046
22. Diltemiz, S. E. r.; Ecevit, K. J. *Alloys Compd.* **2019,** *783*, 608-616. DOI: https://doi.org/10.1016/j.jallcom.2018.12.237

J. Mex. Chem. Soc. **2026**, *70(1):e2490*
Regular Issue

ISSN-e 2594-0317

23. Li, G.; Zhang, W.; Luo, N.; Xue, Z.; Hu, Q.; Zeng, W.; Xu, J. *Nanomaterials.* **2021,** *11*, 1926. DOI: https://doi.org/10.3390/nano11081926
24. Liu, X.; Wang, D.; Li, Y. *Nano Today.* **2012,** *7*, 448-466. DOI: https://doi.org/10.1016/j.nantod.2012.08.003
25. Nguyen, T. T.; Van Dao, D.; Ha, N. T. T.; Van Tran, T.; Kim, D.-S.; Yoon, J.-W.; Ha, N. N.; Lee, I.-H.; Yu, Y.-T. J. S. *Sensors Actuators B: Chem.* **2022,** *354*, 131083.
26. Cai, T.; Zhang, H.; Xing, H.; Xia, X.; Zhang, Z.; Zhang, K.; Chen, H.; Ye, Y.; Guo, W.; Huang, H. J. *J. Electron. Mater.* **2023,** *52*, 4959-4970. DOI: https://doi.org/10.1007/s11664-023-10418-6
27. Zhao, X.; Liu, Y.; Deng, J.; Xu, P.; Yang, J.; Zhang, K.; Han, Z.; Dai, H. *Mol. Catal.* **2017,** *442*, 191-201. DOI: https://doi.org/10.1016/j.mcat.2017.09.002
28. Wu, C. H.; Liu, C.; Su, D.; Xin, H. L.; Fang, H.-T.; Eren, B.; Zhang, S.; Murray, C. B.; Salmeron, M. B. *Nat. Catal.* **2019,** *2*, 78-85. DOI: https://doi.org/10.1038/s41929-018-0190-6
29. Luo, M.; Wang, F.; Liu, Q.; Li, W.; Shao, C.; Liu, X.; Ai, B. *React. Kinet. Mech.* **2023,** *136*, 2039-2051. DOI: https://doi.org/10.1007/s11144-023-02437-5
30. Raveendran, A.; Chandran, M.; Dhanusuraman, R. *RSC Adv.* **2023,** *13*, 3843-3876. DOI: https://doi.org/10.1039/D2RA07642J
31. Ali, S. M. *Sci. Rep.* **2025,** *15*. DOI: https://doi.org/10.1038/s41598-024-84727-z
32. Jin, X.; Zhao, X.; Huang, K. *J. Power Sources.* **2015,** *280*, 195-204. DOI: https://doi.org/10.1016/j.jpowsour.2015.01.080
33. Liu, Y.; Zhang, H.; Ju, A.; Li, P.; Qu, X.J. *J. Energy Storage.* **2024,** *104*, 114731. DOI: https://doi.org/10.1016/j.est.2024.114731
34. Thanh, T. S.; Tu, N. T. T.; Quy, P. T.; Toan, T. T. T.; Thanh, N. M.; Nguyen, V. T.; Tuan, N. H.; Nhiem, D. N.; Lieu, P. K.; Khieu, D. Q. *ECS J. Solid State Sci. Technol***. 2021,** *10*, 117001. DOI: http://dx.doi.org/10.1149/2162-8777/ac372c
35. Eixenberger, J. E.; Anders, C. B.; Hermann, R. J.; Brown, R. J.; Reddy, K. M.; Punnoose, A.; Wingett, D. G. *Chem. Res. Toxicol.* **2017**, *30*, 1641-1651. DOI: https://doi.org/10.1021/acs.chemrestox.7b00136
36. Shubha, J.; Roopashree, B.; Patil, R.; Khan, M.; Shaik, M. R.; Alaqarbeh, M.; Alwarthan, A.; Karami, A. M.; Adil, S. F. *Arab. J. Chem.* **2023**, *16*, 104547-104554. DOI: http://dx.doi.org/10.1016/j.arabjc.2023.104547
37. Al-Rasheidi, M.; Khan, F.; Al-Ahmed, A.; Rehman, S.; Al-Sulaiman, F. *Opt. Mater.* **2022**, *126*, 112144. DOI: https://doi.org/10.1016/j.optmat.2022.112144
38. Chen, Z.; Jaramillo, T. F. J. D. o. C. E. *Chem. Eng. J.* **2017**, *9*, 19.
39. Jubu, P.; Yam, F.; Igba, V.; Beh, K. J. *J. Solid State Chem.* **2020,** *290*, 121576. DOI: https://doi.org/10.1016/j.jssc.2020.121576
40. Li, J.; Yuan, Z.; Mu, Z.; Yang, Z.; Meng, F. J. S. *Sensors Actuators B: Chem.* **2024,** *405*, 135404. DOI: https://doi.org/10.1016/j.snb.2024.135404
41. Ye, L.; Liang, Y. *Physica B.* **2024,** *674*, 415579. DOI: https://doi.org/10.1016/j.physb.2023.415579
42. Hu, Y.; Anandkumar, M.; Joardar, J.; Wang, X.; Deshpande, A. S.; Reddy, K. M. *Sci. Rep.* **2023**, *13*, 2362. DOI: https://doi.org/10.1038/s41598-023-29477-0
43. Ivanova, T.; Maslakov, K.; Sidorov, A.; Kiskin, M.; Linko, R.; Savilov, S.; Lunin, V.; Eremenko, I. *J. Electron. Spectrosc. Relat. Phenom.* **2020,** *238*, 146878. DOI: https://doi.org/10.1016/j.elspec.2019.06.010
44. González-Meza, O.; Larios-Durán, E.; Gutiérrez-Becerra, A.; Casillas, N.; Escalante, J.; Bárcena-Soto, M. *J. ECS Solid State Electrochem.* **2019,** *23*, 3123-3133. DOI: https://doi.org/10.1007/s10008-019-04410-6
45. Lv, J.-J.; Wisitruangsakul, N.; Feng, J.-J.; Luo, J.; Fang, K.-M.; Wang, A.-J. *Electrochim. Acta.* **2015,** *160*, 100-107. V. DOI: https://doi.org/10.1016/j.electacta.2015.02.052
46. Rahman, M. M. *Sensors Actuators B: Chem.* **2020**, *305*, 127541. DOI: https://doi.org/10.1016/j.snb.2019.127541

J. Mex. Chem. Soc. **2026**, *70(1):e2490*
Regular Issue

ISSN-e 2594-0317

47. Xu, S.; Jiang, L.; Huang, X.; Ju, W.; Liang, Y.; Tao, Z.; Yang, Y.; Zhu, B.; Wei, G. *Nanotechnology.* **2023**, *35*, 025704. DOI: http://dx.doi.org/10.1088/1361-6528/ad0124
48. Ma, R.; Wu, F.; Yue, J.; Zhao, W.; Yan, J.; Cui, H.; Feng, P.; Peng, X. *Microchem. J.* **2024**, *205*.DOI: https://doi.org/10.1016/j.microc.2024.111234
49. Becker, A.; Andrikopoulou, C.; Bernhardt, P.; Trocquet, C.; Le Calvé, S., *Chemosensors.* **2020**, *8*. DOI: https://doi.org/10.3390/chemosensors8030057
50. Hornshøj, B. H.; Kobbelgaard, S.; Blakemore, W. R.; Stapelfeldt, H.; Bixler, H. J.; Klinger, M. *Food Addit. Contam. A.* **2015**, *32*, 152-160. DOI: https://doi.org/10.1080/19440049.2014.992049
51. de Freitas Rezende, F. B.; Cheibub, A. M. d. S. S.; Netto, A. D. P.; de Carvalho Marques, F. *Microchem. J.* **2017,** *134*, 383-389.
52. Shin, J.; Jeong, B.; Chinannai, M. F.; Ju, H. *Electrochim. Acta.* **2021**, *390*, 138858. DOI: https://doi.org/10.1016/j.electacta.2021.138858